

Full length article

Thickness dependent response of domain wall motion in declamped {001} Pb(Zr_{0.3}Ti_{0.7})O₃ thin films

Lyndsey M. Denis^{a,*}, Giovanni Esteves^b, Julian Walker^a, Jacob L. Jones^b, Susan Trolier-McKinstry^a

^a Department of Materials Science and Engineering and Materials Research Institute, The Pennsylvania State University, University Park, PA, 16802, USA

^b Department of Materials Science and Engineering, North Carolina State University, Raleigh, NC, 27606, USA

ARTICLE INFO

Article history:

Received 8 December 2017

Received in revised form

22 March 2018

Accepted 23 March 2018

Available online 31 March 2018

Keywords:

Thin films

Size effects

Rayleigh

Dielectric response

Substrate clamping

ABSTRACT

Scaling effects were investigated in tetragonal {001} textured Pb(Zr_{0.3}Ti_{0.7})O₃ thin films doped with 2 mol% Nb over a thickness range of 0.27 μm–1.11 μm. Scaling effects refer to the size-induced degradation of properties at length scales exceeding those associated with the ferroelectric stability limit. The irreversible Rayleigh coefficient was found to be thickness-dependent, indicating suppression of the extrinsic contributions to the relative permittivity for all clamped films. Both defects in the seed layer and substrate clamping contributed to the observed thickness dependence. The influence of the seed layer on dielectric properties was accounted for using a capacitor in series model. After the films were partially declamped from the substrate, the irreversible contributions increased up to 23% in Nb-doped films and became more frequency dependent (by up to 29%). The suppressed frequency dependence in the clamped films was attributed to the pinning of irreversible domain walls active at lower frequencies. Both the seed layer and substrate clamping contributed to the pinning of irreversible domain walls.

© 2018 Acta Materialia Inc. Published by Elsevier Ltd. All rights reserved.

1. Introduction

Ferroelectric thin films such as Pb(Zr_xTi_{1-x})O₃ (PZT) have high dielectric and piezoelectric properties which can be utilized in actuators, sensors, transducers, and energy harvesters in microelectromechanical systems (MEMS) [1,2]. A small film thickness is necessary when high capacitance density (including thin film multilayer ceramic capacitors) or low voltage operation is required [3–5]. However, thickness-dependent property degradation limits the extent that the film thickness can be reduced while maintaining the performance of such devices [6,7].

Scaling effects are the size-induced degradation of piezoelectric, ferroelectric and dielectric properties at length scales (typically between 10 nm and 1 μm) exceeding those associated with the thermodynamic stability limits for a ferroelectric phase (~1 nm) [7,8]. Scaling effects in ferroelectric films are caused by: substrate clamping, residual stresses, dislocations, interfacial passive layers, electrode screening, depolarization fields, changes in grain size, a

higher concentration of defects at the film-substrate interface, or thickness-dependent changes in the domain wall population and/or changes in the domain wall mobility [9–15]. Additionally, scaling effects can be exacerbated by processing. Conversely, size effects are caused by the suppression of the intrinsic contribution to the material response as length scales approach the limits of thermodynamic stability for a ferroelectric phase (~1 nm). Examples of suppressed intrinsic contribution include the reduction of ferroelectric distortions, polarization, piezoelectric coefficients, and permittivity.

Scaling effects are manifested in the degradation of the longitudinal piezoelectric coefficient and relative permittivity as a function of film thickness. This phenomenon is evident for both epitaxial and polycrystalline ferroelectric films of various compositions [7]. In most Pb-based perovskites, the relative permittivity ($\epsilon_{r,33}$) starts to decay significantly below a film thickness of ~100 nm; however, in some cases, gradual decreases in the permittivity start in films as thick as ~1 μm [16]. Since the degradation of $\epsilon_{r,33}$ occurs at film thicknesses much greater than the ferroelectric stability limit, the property degradation at these length scales is attributed to extrinsic scaling effects [17,18]. In particular, it is observed that ferroelastic non-180° domain wall motion is suppressed as thickness decreases.

* Corresponding author. The Pennsylvania State University, N-256 Millennium Science Complex, University Park, PA, 16802, USA.

E-mail address: lmd342@psu.edu (L.M. Denis).

The nonlinearity in the relative permittivity along with the hysteresis in the polarization can be quantified at sub-coercive, alternating current (ac) electric fields using the Rayleigh law, Eqns. (1) and (2) [19,20].

$$P(E) = (\epsilon_{\text{initial}} + \alpha_e E_0) E \pm \frac{\alpha_e}{2} (E_0^2 - E^2) \quad (1)$$

$$\epsilon_r = \epsilon_{\text{initial}} + \alpha_e E_0 \quad (2)$$

Equation (1) describes the nonlinear dependence of the polarization (P) on the driving field (E), where $E = E_0 \sin(\omega t)$, E_0 is the driving field amplitude, $\epsilon_{\text{initial}}$ is the reversible dielectric Rayleigh coefficient and α_e is the irreversible Rayleigh coefficient. $\epsilon_{\text{initial}}$ arises from the reversible extrinsic contributions as well as the intrinsic contributions to the permittivity. α_e is associated with the irreversible movement of interfaces, i.e. domain walls or phase boundaries over a potential energy barrier within a random potential energy landscape [20].

Numerous reports on PZT 52/48 [21–26] and PZT 30/70 [27] demonstrate that the α_e decreases in films of thicknesses below $\sim 1 \mu\text{m}$, indicating that the irreversible domain wall motion contribution to the permittivity is suppressed. These prior results were obtained for continuous films on rigid substrates. However, in many MEMS devices, the film is at least partially released. The release state may change the thickness dependence of α_e and associated scaling effects, since substrate clamping is known to suppress the extent of non- 180° domain wall motion in ferroelectric thin films [28,29]. Therefore, there is a need to investigate the influence of substrate clamping on the thickness-dependent extrinsic contribution to the relative permittivity.

For a fixed film thickness, the clamping of the film can be alleviated in several ways. First, island structures with high aspect ratios allow the structures to be partially de-clamped, thus, increasing 90° domain wall mobility and doubling the remanent polarization of PZT at high applied electric fields [28,30]. Additionally, piezoelectrically-active, ferroelectric nanotubes with high aspect ratios have been created via vacuum infiltration of macroporous Si templates (aspect ratio of $>10:1$) [31] or a bottom-up nanomanufacturing method (aspect ratio of $5:1$) [32]. The high aspect ratios in these studies were chosen such that substrate clamping effects could be minimized. Declamping can also be achieved by releasing diaphragm structures from the underlying substrate [33,34]. The resulting increase in dielectric properties were attributed to lower potential energy barriers which allowed enhanced irreversible domain wall motion and an increase in α_e for the released film. Synchrotron diffraction of films $>1 \mu\text{m}$ in thickness demonstrate that released films show higher levels of non- 180° domain reorientation under field [29]. However, released cantilevers still demonstrate thickness dependent remanent polarization and piezoelectric properties attributed to residual stresses. These residual stresses are commonly associated with the thermal expansion coefficient mismatch between the film and the substrate and/or the presence of a thin layer at the film-substrate interface with a low dielectric constant [35]. In this work, scaling effects have been investigated in PZT films $<1 \mu\text{m}$ thick in both clamped and partially released states relevant to MEMS devices.

2. Experimental procedure

2.1. Film synthesis and nanofabrication

Tetragonal, {001} textured polycrystalline $\text{Pb}(\text{Zr}_{0.3}\text{Ti}_{0.7})\text{O}_3$ (PZT 30/70) thin films doped with 2% Nb were fabricated via chemical solution deposition (CSD) as described elsewhere [36,37]. The

solution was deposited onto a Pt/TiO₂/SiO₂/Si stack to produce films with thickness ranging from 0.27 to 1.11 μm . Prior to the deposition of the film, a 0.08 M PbO layer was spin coated onto the Pt then dried (1 min. at 150°C and 2 min. at 250°C) and pyrolyzed (10 min. at 400°C). This PbO layer was not crystallized. The underlying layer of PbO provided excess lead at the film-substrate interface which minimized lead loss to the substrate during crystallization. A commercial PZT-E1 sol-gel solution (Mitsubishi Materials Corporation, Tokyo, Japan) of composition $\text{Pb}(\text{Zr}_{0.3}\text{Ti}_{0.7})\text{O}_3$ with 10 mol% lead excess, doped with 1 mol% Mn and a concentration of 10 wt% PZT was used to promote {001} texturing. This solution was deposited onto the PbO layer at 2000 rpm, dried (2 min. at 150°C), pyrolyzed (5 min. at 300°C), and crystallized in a rapid thermal annealer (RTA) (1 min. at 700°C in flowing O₂ gas at 2 SLPM and a ramp rate of 10°C/s). As shown in Supplemental Fig. 1, a spin speed of 2000 rpm produced the best {001} texturing of the seed layer; this corresponds to a seed layer thickness of $\sim 60 \text{ nm}$. Above this critical thickness, {111} texture developed; below this critical thickness, {110} texture was observed. Similar results have been obtained for seeding of undoped PZT 52/48 films from Mitsubishi Materials solutions [38,39].

After the crystallization of the seed layer, 0.4M PZT 30/70 sol-gel with 12 mol% lead excess and doped with 2 mol% Nb was spin coated at either 3000 rpm or 1500 rpm, dried (2 min. at 250°C), pyrolyzed (5 min. at 400°C), crystallized in the RTA (1 min. at 700°C in flowing O₂ gas at 2 SLPM and a ramp rate of 10°C/s) and repeated until the desired overall film thickness was obtained. To obtain high quality films with similar grain size distributions, the processing conditions were optimized for the desired film thickness as needed. As the overall film thickness decreases, the number of deposited layers must be decreased to keep the spin speed and layer thickness constant. However, as the number of deposited layers decreases, there is an increased probability of forming a pin hole in the film which will result in a decreased electrode yield. To combat this, the number of deposited layers was increased in thinner films ($<0.56 \mu\text{m}$ thick). Increasing the spin speed from 1500 rpm to 3000 rpm decreased the thickness of each deposited layer and allow more layers to be deposited for a given film thickness. This method was also employed by Bastani et al. to obtain thin insulating PZT films [11]. Supplemental Fig. 2 shows a schematic of the thickness series. The long pyrolysis step enabled the growth of high-density films with lateral grain sizes of 50–150 nm, as shown in Supplemental Fig. 3 which includes field emission scanning electron microscopy (FESEM) images for each film thickness in the series.

To provide excess lead to the surface of the film, after every 5 crystallized layers of PZT 30/70, 0.08M PbO layer was spin coated at 6000 rpm, dried (1 min. at 150°C and 2 min. at 250°C) and crystallized in the RTA (1 min. at 700°C in flowing O₂ gas at 2 SLPM and a ramp rate of 10°C/s). The PbO crystallization steps are also shown in Supplemental Fig. 2, labeled as 'PbO cap'. This converted lead-deficient surface pyrochlore (or fluorite) phases to the desired perovskite phase [40], and improved {001} texturing for both series of samples.

Large area platinum top electrodes ($3.5 \text{ mm} \times 0.7 \text{ mm}$) were defined photolithographically and sputtered onto the PZT using RF magnetron sputtering. Part of the electroded area of the films was released from the substrate by dry etching $600 \mu\text{m} \times 146 \mu\text{m}$ pits through the Pt/PZT/Pt/TiO₂/SiO₂ stack using an Ulvac NE-550 inductively coupled high-density plasma etch tool. The exposed Si substrate was then etched via an isotropic Xactic XeF₂ e1 vapor etch tool until a 100 μm diameter trench was formed, as discussed elsewhere [29,33]. The conditions of the etch recipes for these two steps are listed in Table 1. The sample was annealed at 400°C for 30 min before and after the XeF₂ etch step to remove residual

Table 1
Etch conditions for released structures.

Material	Chamber Pressure	Gas Chemistry	Forward Power	Etch Rate
Pt/PZT/Pt/TiO ₂	5 mTorr	30 sccm Cl ₂ 40 sccm Ar	300 W at MHz 0 W at MHz	Pt: 1500 s/μm PZT: 300 s/μm
SiO ₂	5 mTorr	50 sccm CF ₄	300 W at MHz	240 s/μm
Si	2 mTorr	XeF ₂	–	6 s/μm

moisture and reduce etch damage. The density of the etch pits within one electroded area dictated the percent of electroded area that was released from the substrate (fully clamped or 0% released, 25% released, 50% released and 75% released), as illustrated in Fig. 1 (a). The suspended electroded area above the trench represents a declamped region of the film, shown in Fig. 1 (b). An optical microscope image of the top down view of a released electrode and a cross-sectional FESEM micrograph of the released Pt/PZT/Pt/TiO₂/SiO₂ stack suspended above the etch trench are shown in Fig. 1 (c) and (d), respectively.

2.2. Characterization

The orientation and phase of the film was determined from X-ray diffraction (XRD) patterns taken using a lab source diffractometer (PANalytical Empyrean), as shown in Fig. 2 (a, b). Lotgering factors ranged from 90% to 100% depending on the film thickness, with Lotgering factors closer to 100% for films below ~0.5 μm. The volume fraction of *c*-domains (ν_{002}) of a sample in the as-processed state was calculated from the integrated intensities of the 002 and 200 XRD peaks using LIPRAS (Line-Profile Analysis Software) [41]. An

example of the peak fitting for the 1.1 μm film is shown in Fig. 2 (c) and the corresponding ν_{002} values are shown in Fig. 2 (d). The peaks were fit using an asymmetric Pearson VII function which takes into account the peak asymmetry and approximates the diffuse scattering [42]. ν_{002} was calculated using Equation (3), as described elsewhere [43,44].

$$\nu_{002} = \frac{I_{002}}{I_{002} + 2I_{200}} \tag{3}$$

The term I_{hkl} represents the integrated intensity of the *hkl* reflection determined from the peak fit. I'_{hkl} represents the reference intensity from the powder diffraction file ($I'_{002}=109$ and $I'_{200}=249$) [45]. By using the ratio of integrated intensities over a reference intensity, the structure factors for the 002 and 200 reflections in a tetragonal system are accounted for. Error of ν_{002} was calculated using an error propagation method that accounts for the integrated intensity error generated from peak fitting using LIPRAS.

Polarization vs. electric field (P–E) hysteresis loops were measured at a frequency of 10 Hz using a Radiant Precision

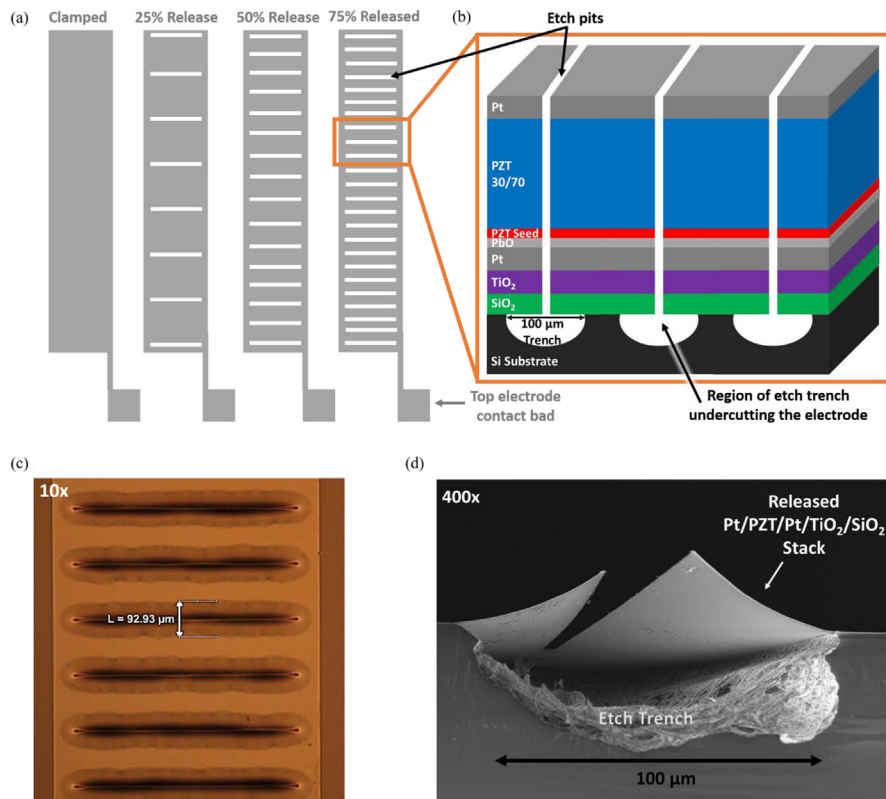


Fig. 1. (a) A top down view of the Pt electrode for each release state: clamped or 0% released, 25% released, 50% released and 75% released. The different degrees of release were achieved by varying the density of the etch pits within one electroded region. (b) 3-D cross-sectional schematics of the release structures including the etch pits that run vertically through the Pt/PZT/Pt/TiO₂/SiO₂ stack and the 100 μm diameter etch trench that was undercut into the Si substrate below each etch pit region (not to scale). (c) An optical microscope image of the top down view of part of a released electrode and (d) a cross-sectional micrograph of the released Pt/PZT/Pt/TiO₂/SiO₂ stack suspended above the etch trench.

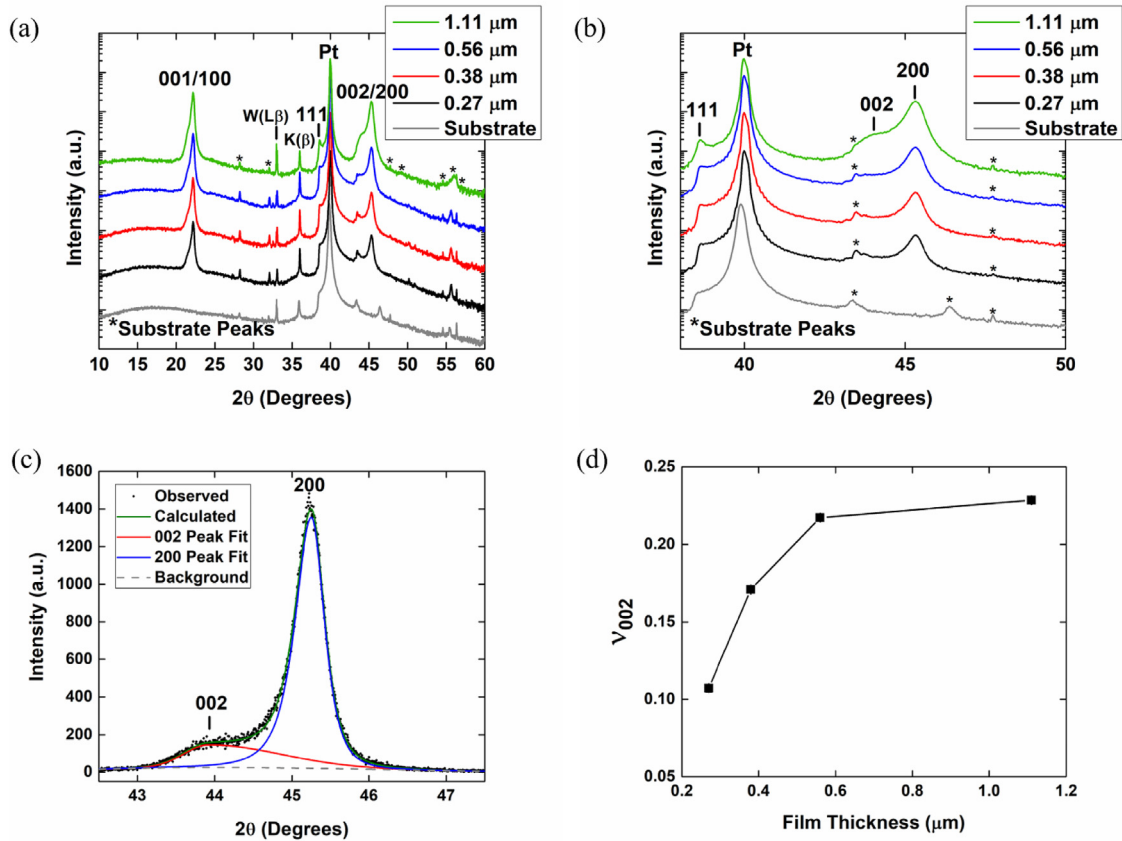


Fig. 2. Phase pure X-ray diffraction patterns of tetragonal {001} textured PZT 30/70 thin films doped with 2% Nb and thicknesses ranging from 0.27 μm to 1.1 μm (a, b). The peak fitting of the 002/200 peaks for the 1.1 μm film is shown (c). The change in the volume fraction of *c*-domains (ν_{002}) is also shown as a function of film thickness (d). Note: error bars are smaller than the symbol size.

Ferroelectric Tester for both clamped films and 75% released films. Further electrical characterization in the form of Rayleigh analysis was conducted on both clamped and released films at frequencies ranging from 50 Hz to 4 kHz with applied AC electric fields up to $0.5 \cdot E_c$ (where E_c is the coercive field). These measurements were taken using a *Hewlett Packard 4284A LCR meter*. The samples were subject to an anneal at 400 °C for 30 min. and an aging time of 24 h prior to the Rayleigh measurements. The aging process was consistent across all samples prior to Rayleigh analysis. Error was calculated using an error propagation method that accounts for the error associated with a 95% confidence interval of the linear fit of the Rayleigh parameter as a function of applied AC electric field.

2.3. Capacitor in series model

To minimize the influence that the seed layer has on the Rayleigh analysis, a capacitor in series model was applied to the permittivity data, as shown in Equation (4) in terms of capacitance (C) and Equation (5) in terms of the dielectric constant (k).

$$\frac{1}{C} = \frac{1}{C_f} + \frac{1}{C_s} \quad (4)$$

$$\frac{k}{t} = \frac{k_f}{t_f} + \frac{k_s}{t_s} \quad (5)$$

where C represents the measured capacitance, C_s is the measured capacitance of the seed layer, C_f is the capacitance of the balance of

the ferroelectric film and t is the total thickness [11,46–49]. C_s was not extracted from a linear relationship between C^{-1} vs. film thickness at zero thickness. Since the volume fraction of *c*-domains is not constant as a function of film thickness, the standard extrapolation will not accurately predict the interface capacitance, since it does not account for the thickness-dependent change of domain state. Rather, C_s is the capacitance of the seed layer, measured as a function of ac electric field for frequencies ranging from 50 to 4000 Hz, as shown in [Supplemental Fig. 4 \(a\)](#). Dispersion curves of the Rayleigh parameters for the seed layer are also reported in [Supplemental Fig. 4 \(b\)](#). The seed layer has a measured dielectric constant of 510 (measured at 1 kHz and 30 mV), which is ~25% less than that of the 0.35 μm PZT film of the same composition and measurement conditions. To check the quality of the Mitsubishi Materials solution used for the seed layer, a 0.38 μm thick film was grown using this solution. The measured Rayleigh parameters of the Mitsubishi Materials 0.38 μm film were comparable to that of a 2-MOE-based sol gel film of thickness 0.38 μm , shown in [Supplemental Fig. 5](#), for the same composition and a common seed layer. This comparison indicates that the suppressed properties of the 0.06 μm seed layer, shown in [Supplemental Fig. 4 \(b\)](#), are due to scaling effects.

3. Results

3.1. Thickness dependence of polarization hysteresis in de-clamped films

[Fig. 3](#) shows the P-E loops for the 2% Nb-doped PZT 30/70

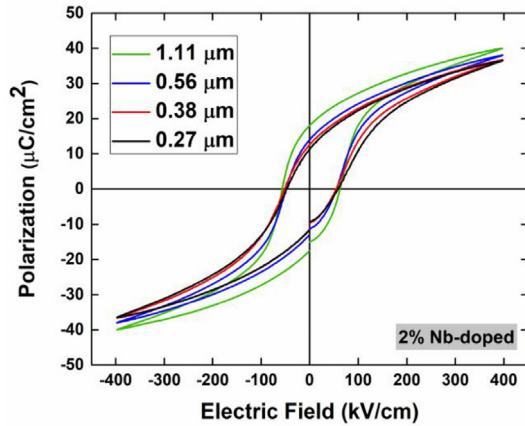


Fig. 3. Polarization vs. electric field hysteresis loops of clamped 2% Nb-doped PZT 30/70 thin films of varying thickness ranging from 0.27 μm to 1.1 μm .

thickness series. The coercive field (E_c) ranges from 54 to 63 kV/cm. The films exhibited remanent polarization (P_r) values ranging from 11 to 18 $\mu\text{C}/\text{cm}^2$. P_r is defined here to be the polarization remaining in the material when the electric field is reduced to zero after applying a maximum electric field of 400 kV/cm in the electric field direction positive direction. The relatively small polarizations are a result, in part, of the largely a -domain state of the films resulting from the thermally induced tensile stress state of the PZT film grown on a Si substrate [50]. In general, as film thickness increases, the maximum polarization (P_{max}) and P_r increase, characteristic of the scaling effect. Upon release, P_r and P_{max} both increase for a given thicknesses, as shown in Fig. 4 for (a) 1.11, (b) 0.38 and (c) 0.27 μm 2% Nb-doped films. This is most clearly seen in Fig. 4 (b), which shows the changes in the P–E loop of 0.38 μm film for each release state (0%, 25%, 50% and 75%). Interestingly, the thinnest film (0.27 μm) shows the smallest increase in P_r after being 75% released from the substrate. This suggests that other mechanisms are involved in pinning domains in the film (e.g., potentially higher defect concentrations, higher grain boundary concentrations, or higher residual stresses in the film that are not relieved upon release).

3.2. Irreversible contributions to permittivity

3.2.1. Thickness dependence in clamped films

Rayleigh analysis was used to characterize extrinsic contributions to the relative permittivity in the form of irreversible domain wall motion. For clamped Nb-doped films, the irreversible contribution to the permittivity, α_e , decreases as film thickness decreases with thickness ranging from 1.11 μm to 0.27 μm . This thickness dependence of α_e is shown in Fig. 5 (a).

Rayleigh parameters of the PZT film, after application of the capacitor-in-series model, were calculated for each film thickness. For simplicity, the Rayleigh parameters prior to applying the capacitor in series model are labeled as ‘Seed + Film’ in Fig. 5 (a), and the data after applying the capacitor in series model are labeled as ‘Film’ in Fig. 5 (b). For the Nb-doped films, the seed layer has a large effect on the irreversible Rayleigh coefficient. The α_e for the PZT film alone is 51% larger than the α_e measured for the film in series with the seed layer. The difference in α_e occurs over the entire frequency range for each film thickness.

Without the influence of the seed layer, α_e values for the 1.11 and 0.56 μm films converge, which suggests that these films have comparable domain wall pinning effects. However, the thickness dependence of α_e is still present in thicknesses below 0.56 μm .

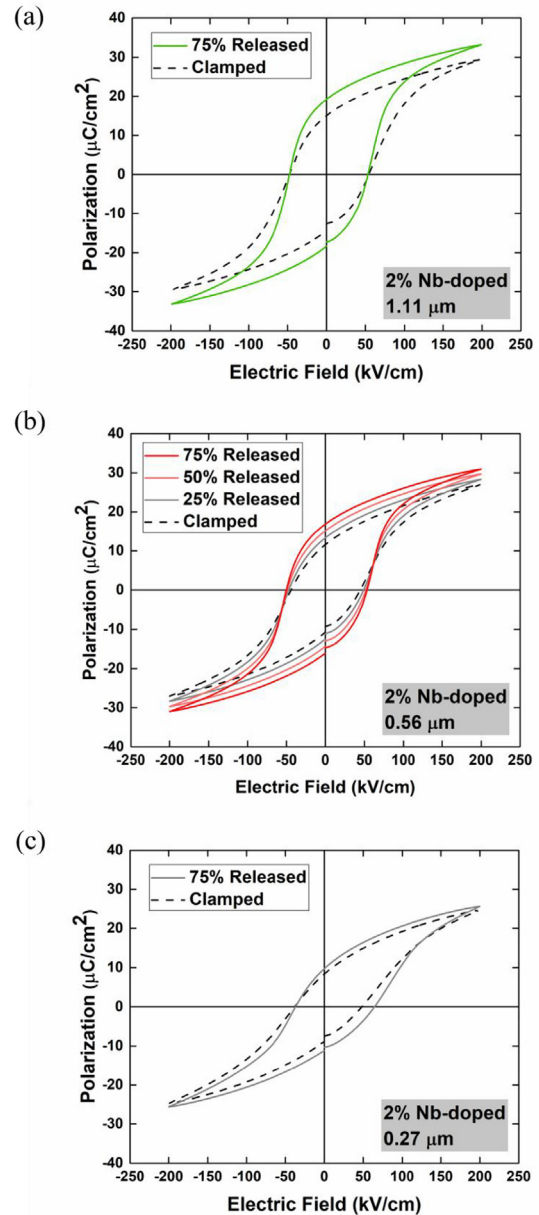


Fig. 4. The change in P–E hysteresis loops of 2% Nb-doped PZT 30/70 thin films between the clamped and 75% released states for (a) 1.11 μm , (b) 0.38 μm , and (c) 0.27 μm thick films. The evolution of the P–E loop for the 0.38 μm thick film is also shown for clamped, 25%, 50% and 75% released states.

Additionally, the α_e values for the 1.11 and 0.56 μm films are lower than those for 0.38 and 0.27 μm films at low frequencies. The origin of this difference is unknown but could be related to a difference in stress level associated with the domain state.

3.2.2. Thickness dependence in released films

To assess whether the suppression of α_e is influenced by substrate clamping, Rayleigh parameters were obtained for films that were partially released from the substrate. Prior to the Rayleigh measurements, the films were subject to high applied electric fields (up to $3E_c$) to induce tearing of the diaphragms and create globally released regions [29]. All films exhibited tearing of the diaphragms with variations in the number of tears and the angle of the tear with respect to the horizontal length of the etch pits. However, most

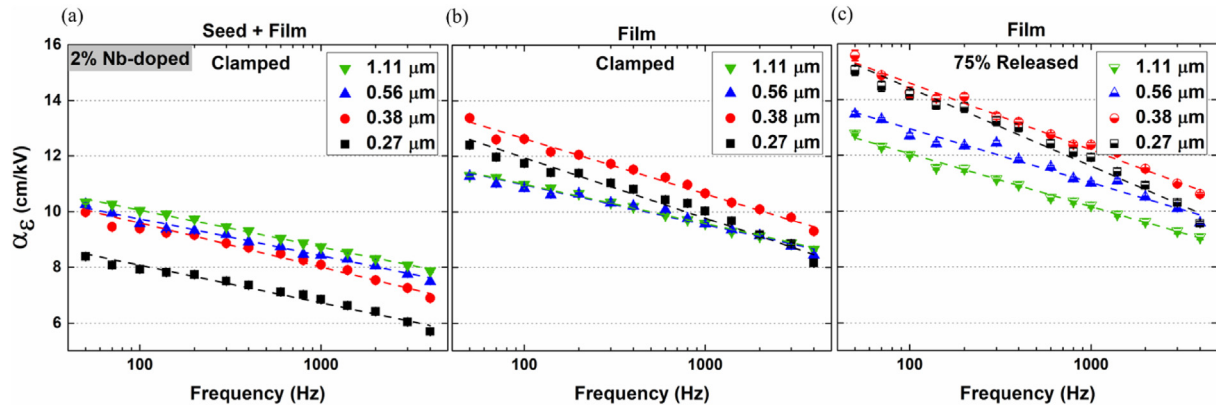


Fig. 5. Frequency dispersion of the Rayleigh parameter α_e as a function of film thickness ranging from 0.27 μm to 1.1 μm for PZT 30/70 thin films doped with 2% Nb in the clamped state before applying the capacitor in series model (Seed + Film) (a), in the clamped state after applying the model (Film) (b) and in the 75% released state after applying the model (c).

electrodes have one tear at each end of the diaphragm regardless of film thickness. The tear typically occurs at the curved ends of the rounded, beam-like etch pits and propagates horizontally towards the electrode edges, shown in the FESEM micrographs of Supplemental Fig. 6. *In situ* synchrotron XRD measurements confirm that, upon global release, enhanced ferroelastic reorientation occurs in PZT 30/70 thin films compared to either local released or clamped states. The enhanced properties in a globally released film are due to the reduction in the average, global tensile stress of the film [29]. After global release, all samples were annealed at 400 °C for 30 min. and aged for 24 h prior to Rayleigh analysis.

To isolate the influence of substrate clamping on the thickness dependence, the trends in α_e were analyzed for a 75% released film after applying the capacitor in series model. Upon 75% release, α_e increases by up to 23%, with larger changes for the thinner films, shown in Fig. 5 (c) for Nb-doped films. Additionally, the evolution of α_e with increasing release state is shown for 0.27 μm 2% Nb-doped film in Fig. 6.

3.3. Frequency dependence of α_e

After applying the capacitor in series model to a clamped Nb-doped film, the greatest increase in α_e occurs at low frequencies, shown in Fig. 7. This indicates that changes in α_e are also frequency-dependent as well as thickness-dependent. The frequency

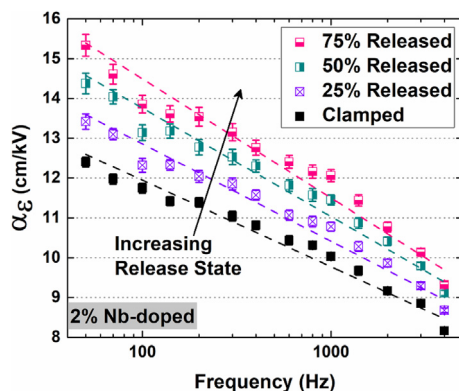


Fig. 6. Frequency dispersion of the Rayleigh parameter α_e as a function of release state including clamped or 0% released, 25% released, 50% released and 75% released from the substrate for 0.27 μm thick PZT 30/70 thin film doped with 2% Nb.

dependence (B_{α_e}) of the Rayleigh coefficient α_e was extracted from fits to Equation (6).

$$\alpha_e = \alpha_{e,i} - B_{\alpha_e} \log f \quad \text{for frequencies in Hz} \quad (6)$$

After applying the capacitor in series model, B_{α_e} increases, shown in Fig. 7 (a) for Nb-doped films. Additionally, larger changes in B_{α_e} are observed for films below 0.5 μm in thickness. This is highlighted in the comparison between the 0.27 μm and 0.54 μm films, shown in Fig. 7 (b–c). A ~69% increase in the frequency dependence of α_e occurs for a 0.27 μm Nb-doped film (b) compared to a ~8% increase for 0.56 μm Nb-doped film (c).

Upon 75% release from the substrate, B_{α_e} increases further for all film thicknesses, as shown in Fig. 7 (a) for Nb-doped films. Upon release, a greater increase in α_e occurs at low frequencies, resulting in an increase in B_{α_e} . However, the change in B_{α_e} upon release does not vary greatly with film thickness.

3.4. Intrinsic and reversible contributions to permittivity

3.4.1. Thickness dependence in clamped films

The thickness dependence in the intrinsic response and the reversible contributions to the dielectric response is represented in the Rayleigh parameter $\varepsilon_{\text{initial}}$. For clamped Nb-doped PZT films, $\varepsilon_{\text{initial}}$ varies non-monotonically as a function of film thickness, shown in Fig. 8 (a), presumably because of differences in the film domain state. The volume fraction of *c*-domains (ν_{002}) increases from 0.11 to 0.23 as film thickness increases from 0.27 to 1.11 μm for 2% Nb-doped films, as shown in Fig. 2 (c). This higher concentration of *c*-domains in thicker films is consistent with findings from the literature [51]. The resulting decrease in the intrinsic contribution to the relative permittivity is reflected in the decrease in the $\varepsilon_{\text{initial}}$ above 0.38 μm .

Rayleigh parameters for clamped, Nb-doped PZT films without the influence of the seed layer are shown in Fig. 8 (b). $\varepsilon_{\text{initial}}$ increases after the applying the capacitor in series model by up to 13%. $\varepsilon_{\text{initial}}$ values for the 0.56, 0.38 and 0.27 μm films approach convergence, suggesting that the films have comparable domain populations, as well as comparable reversible domain wall contributions to $\varepsilon_{\text{initial}}$. However, the 1.11 μm film maintains much lower $\varepsilon_{\text{initial}}$ values due to the greater volume fraction of *c*-domains [52].

3.4.2. Thickness dependence of released films

Fig. 8 (c) shows the influence of 75% release on $\varepsilon_{\text{initial}}$ for the thickness series of Nb-doped films. Upon release, $\varepsilon_{\text{initial}}$ decreases as

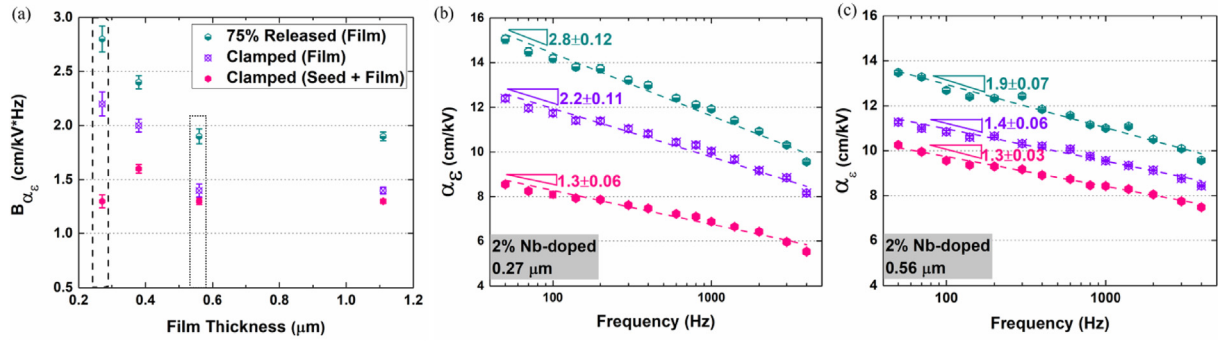


Fig. 7. Frequency dependence (B) of the Rayleigh parameter α_ϵ as a function of film thickness for PZT 30/70 thin films doped with 2% Nb (a) for the clamped state before applying the capacitor in series model (Seed + Film), the clamped state after applying the model (Film), and the 75% release state after applying the model. The dashed and dotted boxes represent values of B_{α_ϵ} for the 0.27 and 0.56 μm films, respectively. Complementary frequency dispersion of the Rayleigh parameter α_ϵ are also shown for thickness 0.27 μm (b) and 0.56 μm (c).

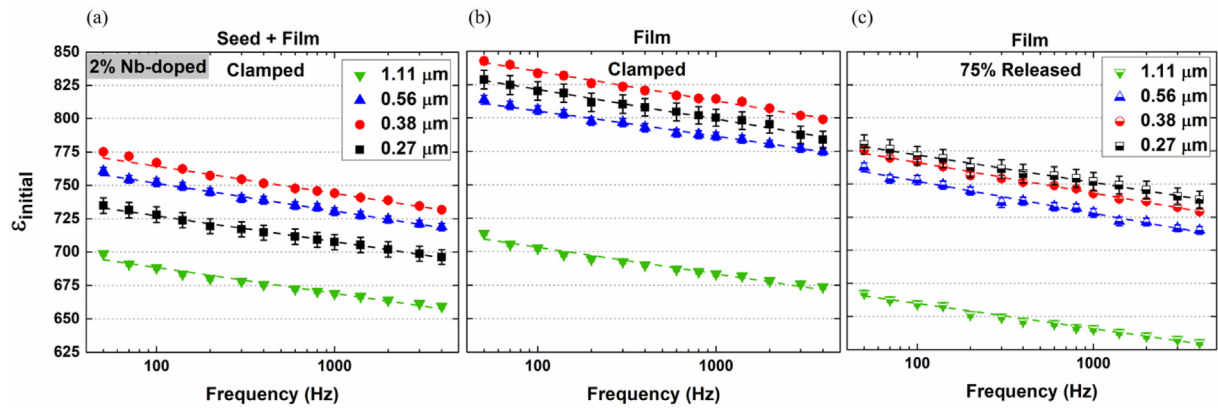


Fig. 8. Frequency dispersion of the Rayleigh parameter $\epsilon_{initial}$ as a function of film thickness ranging from 0.27 μm to 1.1 μm for PZT 30/70 thin films doped with 2% Nb in the clamped state before applying the capacitor in series model (Seed + Film) (a), in the clamped state after applying the model (Film) (b) and in the 75% released state after applying the model (c).

film thickness increases from 0.27 to 1.11 μm . This thickness dependence of $\epsilon_{initial}$ for the 75% released film is influenced by intrinsic contributions, i.e. the change in volume fraction of *c*-domains as a function of thickness, since an increasing volume fraction of *c*-domains will decrease the permittivity.

Interestingly, $\epsilon_{initial}$ decreases with increasing release state for a given film thickness, as shown in Fig. 9 for the 0.27 μm film doped with 2% Nb. It has previously been reported that the release process

itself does not change the volume fraction of *c*-domains at zero applied electric field [29]. Therefore, the observed decrease in $\epsilon_{initial}$ upon release may suggest that there is a shift of at least some of the domain walls from reversible motion in a clamped film to irreversible motion in a released film.

3.5. Frequency dependence of $\epsilon_{initial}$

Removing the influence of the seed layer by applying the capacitor in series model produces little to no change in $B_{\epsilon_{initial}}$, regardless of film thickness, as shown in Supplemental Fig. 7. Upon 75% release from the substrate, there is little to no change in $B_{\epsilon_{initial}}$, regardless of film thickness, also shown in Supplemental Fig. 7. Notably, the changes in B_{α_ϵ} upon release exceed changes in $B_{\epsilon_{initial}}$. The frequency dependence of nonlinearity for α_ϵ and $\epsilon_{initial}$ are listed in Tables II and III in the supplemental information, respectively, for all film thicknesses in the clamped state before the capacitor in series model was applied, the clamped state after the model was applied and the 75% release state after the model was applied.

4. Discussion

4.1. Capacitor-in-series model

The difference in α_ϵ ($\Delta\alpha_\epsilon$) between the total measured response

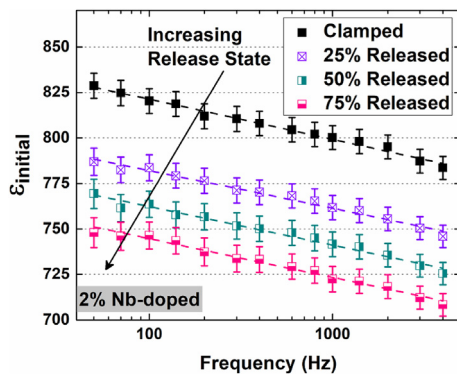


Fig. 9. Frequency dispersion of the Rayleigh parameter $\epsilon_{initial}$ as a function of release state including clamped or 0% released, 25% released, 50% released and 75% released from the substrate for 0.27 μm thick PZT 30/70 thin film doped with 2% Nb.

and the response after applying a capacitor in series model represents the decoupling of the film properties and the seed layer properties, as shown in Fig. 10 (a). The increase in α_e after applying the model suggests that the seed layer contributes directly to the pinning of irreversible domain walls and/or it reduces the field across the balance of the film (which commensurately reduces the domain wall contributions to the properties). Defect dipoles associated with the Mn doping of the seed layer PZT solution, such as $Mn_{Ti}'' - V_O^\bullet$ or $Mn_{Ti}' - V_O^\bullet$, are assumed to be present and create internal electric fields that pin domain walls. Additionally, larger increases in α_e were observed for the thinner films which are more influenced by the seed layer properties in which the seed layer makes up a larger fraction of the total thickness.

For the 1.11 and 0.56 μm films, $\Delta\alpha_e$ is larger at lower frequencies compared to higher frequencies, relating to an increase in B_{α_e} . A larger $\Delta\alpha_e$ at lower frequencies indicates that the seed layer preferentially influences the mobility or density of slower moving irreversible domain walls that are active at lower frequencies. In contrast, $\Delta\varepsilon_{\text{initial}}$ does not vary as a function of frequency, as shown in Fig. 10 (c). $\Delta B_{\varepsilon_{\text{initial}}}$ are representative of changes in the reversible domain wall contributions, as intrinsic contributions should be constant in this frequency range. Therefore, the lack of change in $B_{\varepsilon_{\text{initial}}}$ compared to that for B_{α_e} indicates that the seed layer has a greater impact on irreversible domain wall motion compared to reversible domain wall motion.

4.2. Substrate clamping effects

In general, α_e increases upon 75% release from the substrate. It is

proposed that the potential energy barrier for irreversible domain wall motion decreases upon release, the concentration of pinning sites due to substrate clamping decreases upon release which allows for an increase in domain wall motion, or the mobility of existing domain walls increase. $\Delta\alpha_e$ upon release is greater for thinner films compared to thicker films, as shown in Fig. 10 (b). Strain relaxation upon release from the substrate could be a possible explanation for this trend. Due to the thermal expansion coefficient mismatch between the PZT film and the Si substrate, an in-plane tensile strain in the PZT film develops upon cooling, with a greater amount of thermally-induced strain reported in thinner films compared to thicker films [15]. [53] Variations in the thermal strain as a function of film thickness could also explain the observed change in ν_{002} of a clamped film as film thickness increases.

Additionally, $\Delta\alpha_e$ is larger at lower frequencies compared to higher frequencies, as reflected by an increase in B_{α_e} upon release. This confirms that substrate clamping also preferentially influences the mobility or density of slower moving irreversible domain walls, contributing to the suppression of B_{α_e} . Upon release, either the mobility of the existing domain walls active at lower frequencies rises, or some of the slower moving domain walls are depinned. This is not the case for reversible domain wall motion contributions. Upon release, $\Delta\varepsilon_{\text{initial}}$ does not vary as a function of frequency, as shown in Fig. 10 (d). Since the changes in frequency dependence are representative of changes in the reversible domain wall motion contributions, substrate clamping also has a greater impact on irreversible domain wall motion compared to reversible domain wall motion.

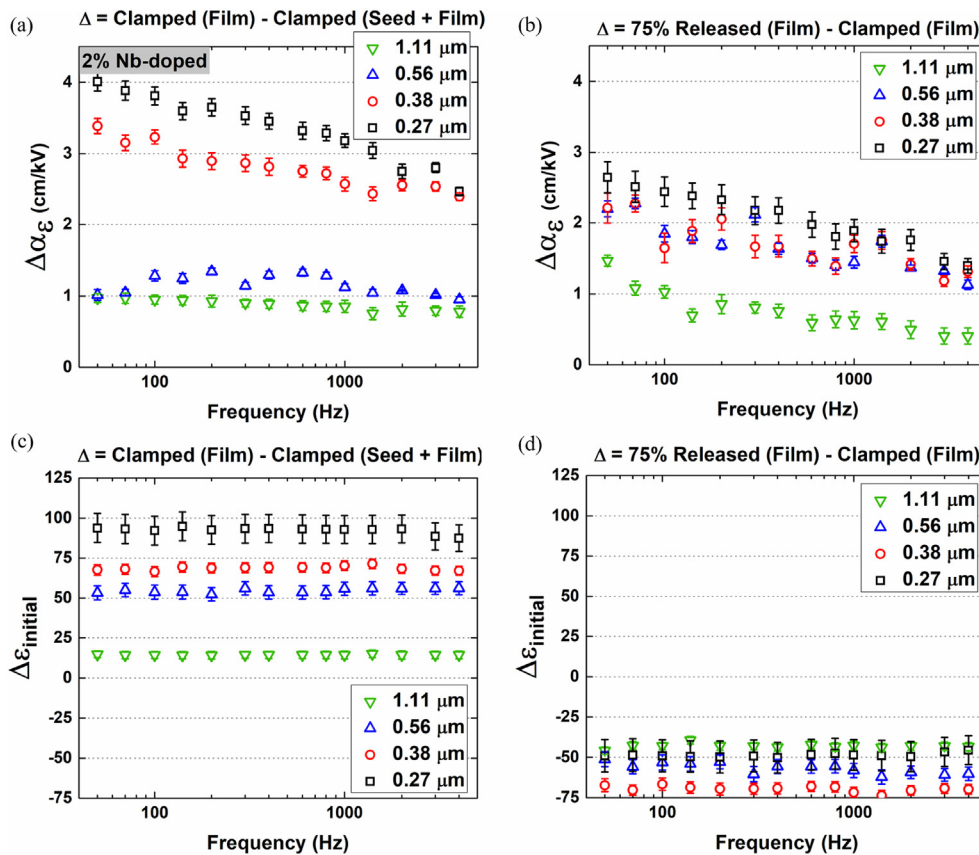


Fig. 10. The change in the Rayleigh parameters α_e (a–b) and $\varepsilon_{\text{initial}}$ (c–d) as a function of film thickness for PZT 30/70 thin films doped with 2% Nb. (a, c) Represents the change after applying the capacitor in series model. (b, d) Represents the change upon release.

5. Conclusions

Rayleigh analysis was used to investigate the influence of substrate clamping on the extrinsic contribution to the relative permittivity of PZT thin films doped with 2% Nb for a film thickness range of 0.27 μm –1.1 μm . These results indicate that both the seed layer and substrate clamping accounted for a substantial apparent suppression of the extrinsic contribution to the relative permittivity. It was found that irreversible domain wall motion contributions to the relative permittivity (α_ϵ) decrease as film thickness decreases, consistent with findings in the literature. The suppression of α_ϵ is partially recoverable by (1) removing the influence of the seed layer via a capacitor in series model and (2) reducing the substrate clamping. The need for a capacitor in series model to account for the seed layer properties will depend explicitly on processing conditions and, therefore, should always be checked. After removing the influence of a Mn-doped seed layer, the α_ϵ for the PZT film alone is 51% larger than the α_ϵ measured for the film in series with the seed layer; this is attributed to the film having a higher irreversible domain wall motion contribution to the permittivity compared to the seed layer. Upon 75% release from the substrate, α_ϵ increased further by up to 23%. Finally, the frequency dependence of α_ϵ increases upon release due to depinning of slower moving irreversible domain walls.

Acknowledgments

The authors gratefully acknowledge funding from the National Science Foundation (DMR-1410907, DMR-1409399) and a National Science Foundation Graduate Research Fellowship Program (DGE-1255832).

Appendix A. Supplementary data

Supplementary data related to this article can be found at <https://doi.org/10.1016/j.actamat.2018.03.046>.

References

- [1] G.L. Smith, J.S. Pulskamp, L.M. Sanchez, D.M. Potrepka, R.M. Proie, T.G. Ivanov, R.Q. Rudy, W.D. Nothwang, S.S. Bedair, C.D. Meyer, R.G. Polcawich, PZT-based piezoelectric MEMS technology, *J. Am. Ceram. Soc.* 95 (2012) 1777–1792, <https://doi.org/10.1111/j.1551-2916.2012.05155.x>.
- [2] P. Muralt, R.G. Polcawich, S. Trolier-McKinstry, Piezoelectric thin films for sensors, actuators, and energy harvesting, *MRS Bull.* 34 (2009) 658–664, <https://doi.org/10.1557/mrs2009.177>.
- [3] M. Randall, D. Skamser, T. Kinard, J. Qazi, A. Tajuddin, S. Trolier-McKinstry, C. Randall, W. Ko, T. Dechakupt, Thin film MLCC, *Cart. 2007 electron, Comp. Assem. Mater. Assoc* (2007) 1–12.
- [4] H. Kishi, Y. Mizuno, H. Chazono, Base-metal electrode-multilayer ceramic capacitors: past, present and future perspectives, *Jpn. J. Appl. Phys.* 42 (2003) 1–15, <https://doi.org/10.1143/JJAP.42.1>.
- [5] D. Newns, B. Elmegreen, X. Hu Liu, G. Martyna, A low-voltage high-speed electronic switch based on piezoelectric transduction, *J. Appl. Phys.* 111 (2012) 84509, <https://doi.org/10.1063/1.4704391>.
- [6] T.M. Shaw, S. Trolier-McKinstry, P.C. McIntyre, The properties of ferroelectric films at small dimensions, *Annu. Rev. Mater. Sci.* 30 (2000) 263–298, <https://doi.org/10.1146/annurev.matsci.30.1.263>.
- [7] J.F. Ihlefeld, D.T. Harris, R. Keech, J.L. Jones, J.-P. Maria, S. Trolier-McKinstry, Scaling effects in perovskite ferroelectrics: fundamental limits and process-structure-property relations, *J. Am. Ceram. Soc.* 99 (2016) 2537–2557, <https://doi.org/10.1111/jace.14387>.
- [8] D.D. Fong, Ferroelectricity in ultrathin perovskite films, *Science* 80 (304) (2004) 1650–1653, <https://doi.org/10.1126/science.1098252>.
- [9] F. Xu, S. Trolier-McKinstry, W. Ren, B. Xu, Z.-L. Xie, K.J. Hemker, Domain wall motion and its contribution to the dielectric and piezoelectric properties of lead zirconate titanate films, *J. Appl. Phys.* 89 (2001) 1336–1348, <https://doi.org/10.1063/1.1325005>.
- [10] L. Pintilie, I. Vrejoiu, D. Hesse, G. LeRhun, M. Alexe, Extrinsic contributions to the apparent thickness dependence of the dielectric constant in epitaxial $\text{Pb}(\text{Zr,Ti})\text{O}_3$ thin films, *Phys. Rev. B* 75 (2007) 224113, <https://doi.org/10.1103/PhysRevB.75.224113>.
- [11] Y. Bastani, T. Schmitz-Kempen, A. Roelofs, N. Bassiri-Gharb, Critical thickness for extrinsic contributions to the dielectric and piezoelectric response in lead zirconate titanate ultrathin films, *J. Appl. Phys.* 109 (2011) 14115, <https://doi.org/10.1063/1.3527970>.
- [12] R.J. Ong, D.A. Payne, N.R. Sottos, Processing effects for integrated PZT: residual stress, thickness, and dielectric properties, *J. Am. Ceram. Soc.* 88 (2005) 2839–2847, <https://doi.org/10.1111/j.1551-2916.2005.00641.x>.
- [13] E.B. Araújo, E.C. Lima, I.K. Bdkin, A.L. Kholkin, Thickness dependence of structure and piezoelectric properties at nanoscale of polycrystalline lead zirconate titanate thin films, *J. Appl. Phys.* 113 (2013) 187206, <https://doi.org/10.1063/1.4801961>.
- [14] V. Nagarajan, J. Junquera, J.Q. He, C.L. Jia, R. Waser, K. Lee, Y.K. Kim, S. Baik, T. Zhao, R. Ramesh, P. Ghosez, K.M. Rabe, Scaling of structure and electrical properties in ultrathin epitaxial ferroelectric heterostructures, *J. Appl. Phys.* 100 (2006) 51609, <https://doi.org/10.1063/1.2337363>.
- [15] T.A. Berfield, R.J. Ong, D.A. Payne, N.R. Sottos, Residual stress effects on piezoelectric response of sol-gel derived lead zirconate titanate thin films, *J. Appl. Phys.* 101 (2007) 24102, <https://doi.org/10.1063/1.2422778>.
- [16] F. Chu, F. Xu, J. Shepard, S. Trolier-McKinstry, Thickness dependence of the electrical properties of sol-gel derived lead zirconate titanate thin films with (111) and (100) texture, *MRS Proc.* 493 (1997) 409, <https://doi.org/10.1557/PROC-493-409>.
- [17] D.-J. Kim, J.-P. Maria, A.I. Kingon, S.K. Streiffer, Evaluation of intrinsic and extrinsic contributions to the piezoelectric properties of $\text{Pb}(\text{Zr}_{1-x}\text{Ti}_x)\text{O}_3$ thin films as a function of composition, *J. Appl. Phys.* 93 (2003) 5568–5575, <https://doi.org/10.1063/1.1566478>.
- [18] J. Pérez de la Cruz, E. Joanni, P.M. Vilarinho, A.L. Kholkin, Thickness effect on the dielectric, ferroelectric, and piezoelectric properties of ferroelectric lead zirconate titanate thin films, *J. Appl. Phys.* 108 (2010) 114106, <https://doi.org/10.1063/1.3514170>.
- [19] D. Damjanovic, M. Demartin, The Rayleigh law in piezoelectric ceramics, *J. Phys. D Appl. Phys.* 29 (1996) 2057–2060, <https://doi.org/10.1088/0022-3727/29/7/046>.
- [20] S. Trolier-McKinstry, N. Bassiri Gharb, D. Damjanovic, Piezoelectric nonlinearity due to motion of 180° domain walls in ferroelectric materials at sub-coercive fields: a dynamic poling model, *Appl. Phys. Lett.* 88 (2006) 202901, <https://doi.org/10.1063/1.2203750>.
- [21] N. Bassiri-Gharb, I. Fujii, E. Hong, S. Trolier-McKinstry, D.V. Taylor, D. Damjanovic, Domain wall contributions to the properties of piezoelectric thin films, *J. Electroceramics* 19 (2007) 49–67, <https://doi.org/10.1007/s10832-007-9001-1>.
- [22] I.F. Fujii, E.H. Hong, S. Trolier-McKinstry, Thickness dependence of dielectric nonlinearity of lead zirconate titanate films, *IEEE Trans. Ultrason. Ferroelectr. Freq. Control* 57 (2010) 1717–1723, <https://doi.org/10.1109/TUFFC.2010.1610>.
- [23] P. Bintachitt, S. Jesse, D. Damjanovic, Y. Han, I.M. Reaney, S. Trolier-McKinstry, S. V Kalinin, T. Nattermann, Collective dynamics underpins Rayleigh behavior in disordered polycrystalline ferroelectrics, *Proc. Natl. Acad. Sci.* 107 (2010) 7219–7224, <https://doi.org/10.1073/pnas.0913172107>.
- [24] W. Zhu, I. Fujii, W. Ren, S. Trolier-McKinstry, Influence of Mn doping on domain wall motion in $\text{Pb}(\text{Zr}_{0.52}\text{Ti}_{0.48})\text{O}_3$ films, *J. Appl. Phys.* 109 (2011) 64105, <https://doi.org/10.1063/1.3552298>.
- [25] C.-R. Cho, W.-J. Lee, B.-G. Yu, B.-W. Kim, Dielectric and ferroelectric response as a function of annealing temperature and film thickness of sol-gel deposited $\text{Pb}(\text{Zr}_{0.52}\text{Ti}_{0.48})\text{O}_3$ thin film, *J. Appl. Phys.* 86 (1999) 2700–2711, <https://doi.org/10.1063/1.371114>.
- [26] A.J. Welsh, R.H.T. Wilke, M.A. Hickner, S. Trolier-McKinstry, Low-cost, damage-free patterning of lead zirconate titanate films, *J. Am. Ceram. Soc.* 96 (2013) 2799–2805, <https://doi.org/10.1111/jace.12505>.
- [27] D.-J. Kim, J.-H. Park, D. Shen, J.W. Lee, A.I. Kingon, Y.S. Yoon, S.-H. Kim, Thickness dependence of submicron thick $\text{Pb}(\text{Zr}_{0.3}\text{Ti}_{0.7})\text{O}_3$ films on piezoelectric properties, *Ceram. Int.* 34 (2008) 1909–1915, <https://doi.org/10.1016/j.ceramint.2007.07.016>.
- [28] V. Nagarajan, A. Roytburd, A. Stanishevsky, S. Prasertchoung, T. Zhao, L. Chen, J. Melngailis, O. Auciello, R. Ramesh, Dynamics of ferroelastic domains in ferroelectric thin films, *Nat. Mater.* 2 (2003) 43–47, <https://doi.org/10.1038/nmat800>.
- [29] M. Wallace, R.L. Johnson-Wilke, G. Esteves, C.M. Fancher, R.H.T. Wilke, J.L. Jones, S. Trolier-McKinstry, In situ measurement of increased ferroelectric/ferroelastic domain wall motion in declamped tetragonal lead zirconate titanate thin films, *J. Appl. Phys.* 117 (2015) 54103, <https://doi.org/10.1063/1.4907394>.
- [30] S. Bühlmann, B. Dwir, J. Baborowski, P. Muralt, Size effect in mesoscopic epitaxial ferroelectric structures: increase of piezoelectric response with decreasing feature size, *Appl. Phys. Lett.* 80 (2002) 3195–3197, <https://doi.org/10.1063/1.1475369>.
- [31] S.S.N. Bharadwaja, M. Olszta, S. Trolier-McKinstry, X. Li, T.S. Mayer, F. Roozeboom, Fabrication of high aspect ratio ferroelectric microtubes by vacuum infiltration using macroporous silicon templates, *J. Am. Ceram. Soc.* 89 (2006) 2695–2701, <https://doi.org/10.1111/j.1551-2916.2006.01123.x>.
- [32] A. Bernal, A. Tselev, S. Kalinin, N. Bassiri-Gharb, Free-standing ferroelectric nanotubes processed via soft-template infiltration, *Adv. Mater.* 24 (2012) 1160–1165, <https://doi.org/10.1002/adma.201103993>.
- [33] F. Griggio, S. Jesse, A. Kumar, O. Ovchinnikov, H. Kim, T.N. Jackson, D. Damjanovic, S.V. Kalinin, S. Trolier-McKinstry, Substrate clamping effects on irreversible domain wall dynamics in lead zirconate titanate thin films,

- Phys. Rev. Lett. 108 (2012) 157604, <https://doi.org/10.1103/PhysRevLett.108.157604>.
- [34] C. Yeager, PZT thin films for piezoelectric MEMS mechanical energy harvesting, Ph.D. Thesis Mater. Sci. Eng. Pennsylvania State Univ. (n.d.).
- [35] M.D. Nguyen, M. Dekkers, H.N. Vu, G. Rijnders, Film-thickness and composition dependence of epitaxial thin-film PZT-based mass-sensors, *Sensors Actuators A Phys.* 199 (2013) 98–105, <https://doi.org/10.1016/j.sna.2013.05.004>.
- [36] N. Ledermann, P. Murali, J. Baborowski, S. Gentil, K. Mukati, M. Cantoni, A. Seifert, N. Setter, {1 0 0}-Textured, piezoelectric Pb(Zr_x, Ti_{1-x})O₃ thin films for MEMS: integration, deposition and properties, *Sensors Actuators A Phys.* 105 (2003) 162–170, [https://doi.org/10.1016/S0924-4247\(03\)00090-6](https://doi.org/10.1016/S0924-4247(03)00090-6).
- [37] S.K. Dey, K.D. Budd, D.A. Payne, Thin-film ferroelectrics of PZT of sol-gel processing, *IEEE Trans. Ultrason. Ferroelectr. Freq. Control* 35 (1988) 80–81, <https://doi.org/10.1109/58.4153>.
- [38] T.M. Borman, S.W. Ko, P. Mardilovich, S.E. Trolier-McKinstry, Development of crystallographic texture in chemical solution deposited lead zirconate titanate seed layers, *J. Am. Ceram. Soc.* 100 (2017) 4476–4482, <https://doi.org/10.1111/jace.15019>.
- [39] T. Doi, H. Sakurai, N. Soyama, Method of forming PNBZT ferroelectric thin film, *Pat. Appl.* (2014) 1–16. EP2784802 A1.
- [40] G.L. Brennecke, C.M. Parish, B.A. Tuttle, L.N. Brewer, M.A. Rodriguez, Reversibility of the perovskite-to-fluorite phase transformation in lead-based thin and ultrathin films, *Adv. Mater.* 20 (2008) 1407–1411, <https://doi.org/10.1002/adma.200702442>.
- [41] G. Esteves, K. Ramos, C.M. Fancher, J.L. Jones, LIPRAS: Line-profile Analysis Software, 2017, pp. 1–4, <https://doi.org/10.13140/RG.2.2.29970.25282/3>.
- [42] J.E. Daniels, J.L. Jones, T.R. Finlayson, Characterization of domain structures from diffraction profiles in tetragonal ferroelastic ceramics, *J. Phys. D Appl. Phys.* 39 (2006) 5294–5299, <https://doi.org/10.1088/0022-3727/39/24/029>.
- [43] J.L. Jones, E.B. Slamovich, K.J. Bowman, Domain texture distributions in tetragonal lead zirconate titanate by x-ray and neutron diffraction, *J. Appl. Phys.* 97 (2005) 34113, <https://doi.org/10.1063/1.1849821>.
- [44] T. Key, J.L. Jones, W.F. Shelley, K.J. Bowman, Quantifying domain textures in lead zirconate titanate using 022:202 and 220 diffraction peaks, *Solid State Phenom.* 105 (2005) 379–384, [10.4028/www.scientific.net/SSP.105.379](https://doi.org/10.4028/www.scientific.net/SSP.105.379).
- [45] International Centre for Diffraction Data, in Card 01-070-4261, (n.d.).
- [46] A.K. Tagantsev, M. Landivar, E. Colla, N. Setter, Identification of passive layer in ferroelectric thin films from their switching parameters, *J. Appl. Phys.* 78 (1995) 2623–2630, <https://doi.org/10.1063/1.360122>.
- [47] A.K. Tagantsev, G. Gerra, Interface-induced phenomena in polarization response of ferroelectric thin films, *J. Appl. Phys.* 100 (2006) 51607, <https://doi.org/10.1063/1.2337009>.
- [48] C. Basceri, S.K. Streiffer, A.I. Kingon, R. Waser, The dielectric response as a function of temperature and film thickness of fiber-textured (Ba,Sr)TiO₃ thin films grown by chemical vapor deposition, *J. Appl. Phys.* 82 (1997) 2497–2504, <https://doi.org/10.1063/1.366062>.
- [49] Y. Xia, J. Wang, Switching behavior of ferroelectric thin films with deadlayers, *Smart Mater. Struct.* 21 (2012) 94019, <https://doi.org/10.1088/0964-1726/21/9/094019>.
- [50] B.A. Tuttle, R.W. Schwartz, Solution deposition of ferroelectric thin films, *MRS Bull.* 21 (1996) 49–54, <https://doi.org/10.1557/S088376940004608X>.
- [51] Z. Wu, J. Zhou, W. Chen, J. Shen, C. Lv, Effects of residual stress on the electrical properties in PbZr_{0.52}Ti_{0.48}O₃ thin films, *J. Sol. Gel Sci. Technol.* 75 (2015) 551–556, <https://doi.org/10.1007/s10971-015-3725-1>.
- [52] M.J. Haun, E. Furman, S.J. Jang, L.E. Cross, Thermodynamic theory of the lead zirconate-titanate solid solution system, part I: phenomenology, *Ferroelectrics* 99 (1989) 13–25, <https://doi.org/10.1080/00150198908221436>.
- [53] S.S. Sengupta, S.M. Park, D.A. Payne, L.H. Allen, Origins and evolution of stress development in sol-gel derived thin layers and multideposited coatings of lead titanate, *J. Appl. Phys.* 83 (1998) 2291–2296, <https://doi.org/10.1063/1.366971>.